ARTICLE IN PRESS

ELSEVIER

Journal of Atmospheric and Solar-Terrestrial Physics ▮ (▮▮▮▮) ▮▮▮–▮▮▮

Journal of ATMOSPHERIC AND SOLAR-TERRESTRIAL PHYSICS

www.elsevier.com/locate/jastp

Initial results from the coupled magnetosphere ionosphere thermosphere model: magnetospheric and ionospheric responses

M. Wiltberger[a,*], W. Wang[a], A.G. Burns[a], S.C. Solomon[a], J.G. Lyon[b], C.C. Goodrich[c]

[a]*National Center for Atmospheric Research, High Altitude Observatory, 3450 Mitchell Lane, Boulder, CO 80301, USA*
[b]*Dartmouth College, Department of Physics and Astronomy, 6127 Wilder Laboratory, Hanover, NH 03755, USA*
[c]*Boston University, Center for Space Weather Modeling, 725 Commonwealth Ave., Boston, MA 02155, USA*

Received 27 January 2004; accepted 19 March 2004

Abstract

The Center for Integrated Space Weather Modeling (CISM) is developing a simulation package of the coupled Sun–Earth system by connecting existing models within each region. The Coupled Magnetosphere Ionosphere Thermosphere (CMIT) model combines the Lyon–Fedder–Mobarry global magnetohydrodynamic (MHD) magnetospheric (LFM) model with the Thermosphere Ionosphere Nested Grid (TING) model. The LFM uses the ideal MHD equations to model the interaction between the magnetospheric plasma and the solar wind. It includes the magnetosphere–ionosphere interaction by requiring the conservation of current flowing between the magnetosphere and a two dimensional ionosphere. TING is a three dimensional code designed to simulate the thermosphere–ionosphere system by solving the mass, momentum, and thermodynamic energy equations for the global thermosphere and ionosphere. Normally, TING uses parameterized models to describe the magnetospheric input into the ionosphere. We begin this paper with a description of how the TING model is used to replace the simple two dimensional ionosphere within the LFM to produce the CISM CMIT Model. The results from the coupled model for a series of steady IMF conditions are compared with the results from the LFM to show that these models have been successfully combined. The problem of high cross polar cap potentials remains, but the structure of the magnetosphere is not dramatically altered by the coupling and the ionospheric conductances show a more realistic distribution driven by EUV radiation as well as a more clearly defined auroral oval.

Keywords: Magnetosphere; Ionosphere; Thermosphere; MHD; Modeling

---

1. Introduction

Study of the complicated regions that make up the connected Sun–Earth system has for the most part been done by first developing models for the individual regions within the system in order to keep the problem tractable. The Center for Integrated Space Weather

---

*Corresponding author. Tel.: +1-303-497-1532; fax: +1-303-497-2180.

E-mail addresses: wiltbemj@ucar.edu (M. Wiltberger), wbwang@ucar.edu (W. Wang), aburns@ucar.edu (A.G. Burns), stans@ucar.edu (S.C. Solomon), lyon@tinman.dartmouth.edu (J.G. Lyon), ccg@bu.edu (C.C. Goodrich).

1364-6826/$ - see front matter © 2004 Elsevier Ltd. All rights reserved.
doi:10.1016/j.jastp.2004.03.026

Modeling (CISM) is using the accomplishments in the separate regions to build a physics based model for the entire system by connecting successful regional models together (see Luhman et al., 2004, for more details). This paper focuses on coupling the magnetosphere to the ionosphere and thermosphere.

Modeling of the magnetosphere is traditionally approached by solving the magnetohydrodynamic (MHD) equations in the near Earth space environment (Lyon et al., 1998; Raeder and McPherron, 1998; Siscoe et al., 2000; Janhunen, 1996; Gombosi et al., 1998). These models are usually set up to take solar wind conditions as upstream and side boundary conditions. Closure of current through the inner boundary, typically placed between two and three earth radii (R_E) requires some type of ionospheric boundary conditions. Early work was done using constant conductance spheres (Fedder and Lyon, 1987) as the boundary condition. As the models became more advanced empirical relationships where used to determine the ionospheric conductivity from particle precipitation and solar EUV radiation (Fedder et al., 1995b; Raeder, 1999). The improvements in ionospheric modeling led to more accurate modeling of substorms (Wiltberger et al., 2000) and storms (Goodrich et al., 1998), but did not fully resolve the three dimensional nature of the ionosphere. The ionospheric model Janhunen (1996) uses within GUMICS is electrodynamic and fully three dimensional. However, none of these magnetospheric models included the effects of the thermosphere on the magnetosphere.

The Earth's thermosphere–ionosphere is a nonlinear dynamical system that interacts with other regions of the Earth's atmosphere through mass, momentum, and energy transfer. Thermosphere–ionosphere general circulation models have been developed to study the global chemical and dynamic processes occurring through out this coupled system (Roble et al., 1998; Richmond et al., 1992; Roble and Ridley, 1994; Fuller-Rowell et al., 1994). All of these models use either empirical models or data assimilation techniques (AMIE, Richmond, 1992) to specify the magnetospheric electric field and particle precipitation inputs at high latitudes. The use of empirical models cuts off the dynamical link between the ionosphere–thermosphere and the magnetosphere and is therefore, in most cases, unable to include the spatio-temporal variability of magnetospheric inputs which are crucial to space weather applications.

Raeder et al. (2001) produced the first fully coupled magnetosphere–ionosphere–thermosphere model by combining the UCLA magnetosphere model with the NOAA Coupled Thermosphere Ionosphere Model (CTIM). Their coupling included using an empirical energetic electron flux within the UCLA model to drive CTIM. The resulting conductances and neutral wind driven currents within CTIM are used to determine the ionospheric potential in the UCLA model. This approach yields a consistent potential in both models while self consistently including the thermospheric feedback driven by the neutral winds. Ridley et al. (2003) coupled the BATSRUS global MHD simulation with the National Center for Atmospheric Research (NCAR) Thermosphere Ionosphere Electrodynamic General Circulation Model (TIEGCM). In their coupling, the conductances are determined by the empirical model within BATSRUS and this information is used by the TIEGCM to determine the wind driven field aligned currents. These currents are fed back into BATSRUS for the determination of the ionospheric potential which is used as the magnetospheric boundary condition. This approach results in a coupling which is not self consistent and may cause the strength of the neutral winds to be underestimated.

In this paper we present initial results from coupling the LFM with thermosphere ionosphere nested grid (TING) to form the CISM Coupled Magnetosphere Ionosphere Thermosphere (CMIT) Model. The following section briefly describes the LFM and TING models and provides a detailed explanation how the models are coupled together. In Section 3, we compare the results of the CMIT model with the stand alone LFM for an idealized set of solar wind conditions which includes 4 h of steady IMF at each of the cardinal magnetic field directions. In the final section of the paper we present a brief discussion of the results and directions for further research.

2. The CISM coupled magnetosphere ionosphere thermosphere model

As part of the model being developed by CISM to study the Sun–Earth Connections we have begun to produce a coupled model of the magnetosphere, ionosphere, and thermospheric portions of the system. This magnetospheric portion of the model uses the Lyon–-Fedder–Mobarry global magnetospheric model. The ionosphere and thermosphere are simulated with the TING model. This section provides a brief outline of each of these models and the process used to couple them together into the CISM CMIT model.

2.1. The Lyon–Fedder–Mobarry global magnetosphere model

The Lyon–Fedder–Mobarry global magnetosphere model (Fedder et al., 1995a; Fedder and Lyon, 1995; Mobarry et al., 1996) solves the ideal MHD equations (Chen, 1984) in a large region around the Earth and couples to an ionospheric simulation as a lower boundary condition. The magnetospheric region can be thought of as a large cylinder $100R_E$ in radius with a front boundary $30R_E$ upstream and a back boundary $300R_E$ downstream. The boundary conditions along the front and sides of the cylinder are the imposed supersonic flow conditions present in the solar wind plasma which propagates through the computational domain. These conditions can be taken from in situ observations made by spacecraft like WIND or ACE. An idealized set of plasma and magnetic field conditions can be used instead of actual solar wind observations. Another option is to extract plasma and magnetic field information at the Earth from a heliospheric code such as ENLIL (Odstrcil et al., 2002). In order to include the effects of dipole rotation, the simulations are performed in solar-magnetic (SM) coordinates, which essentially transfers the dipole rotation into the incoming solar wind stream. The location of the back boundary has been chosen to be far enough downstream to allow the plasma flow to return to its supersonic state as well as being hydromagnetically disconnected from the Earth, so that simple supersonic outflow rules can be used as the boundary conditions.

The ideal MHD equations are solved using the partial donor method (Hain, 1977, 1987) on a grid which has been specially adapted to the magnetospheric problem. The LFM uses a logically rectangular structure but a nonorthogonal set of cells. This grid allows more resolution in regions like the magnetopause, bow shock, and magnetotail which are known a priori require more detail while maintaining the ease of coding provided by a regular layout of cells. It is important to note that the ideal MHD equations do not include the effects of resistivity, which means that reconnection is not possible. The discretization of the equations onto the grid results in a 'numerical' resistivity which allows for reconnection to occur in regions where oppositely directed magnetic fields are forced into a single cell. The work of Fedder and Lyon (1987) and Fedder et al. (1995a) has shown that the rate of reconnection in the magnetosphere is controlled by the solar wind conditions and the coupling with the ionosphere and not by the cell sizes in the simulation.

As previously mentioned the LFM also includes an ionospheric model which is coupled to the magnetospheric calculation. A sphere centered around the Earth is removed from the computational domain. The radius of this boundary is governed by two effects; (1) since the Alfven velocity rapidly increases with decreasing altitude, the closer the boundary is to the Earth the smaller the maximum allowed time step within the magnetosphere becomes and (2) the closer the boundary is to the Earth the larger the extent is of the high latitude ionosphere that can be modeled because lower L-shells map to lower latitudes. In our experience, a sphere of $2R_E$ in radius provides an excellent balance between these two constraints. The field aligned currents (FAC) flowing into the inner boundary are mapped instantaneously along dipole field lines into the ionosphere where current continuity is applied to obtain

$$\nabla_\perp \cdot \bar{\Sigma} \cdot \nabla_\perp \Phi = J_\parallel \tag{1}$$

as a two-dimensional electrostatic model for the ionosphere with Σ as the conductivity tensor, Φ as the electric potential, and $J_\parallel$ as the upward FAC. A more detailed derivation of this equation and its application in the LFM can be found in Wiltberger et al. (2003).

The mapping of the points along the inner boundary of the magnetospheric simulation along dipole field lines to a height of 100 km results in the 2D ionospheric grid shown in Fig. 1. The center of the grid is aligned with the magnetic pole and the lower boundary matches the dipole mapping from the inner boundary of the magnetospheric grid, which is approximately 45° for simulations with a $2R_E$ inner boundary. The cells in the ionospheric grid are roughly rectangular over the majority of the ionosphere and for this resolution are approximately 400×400 km in size. Another advantage of this grid is that it removes the problem of the topological singularity at the pole, which is common in most circular (r, θ) grids. The cell size is not uniform and becomes very small at regions located near noon and midnight at the lowest latitudes. In order to solve Eq. (1) a series of guard cells outside the low latitude boundary is constructed and the potential is assumed to be zero.

The determination of the anisotropic conductance tensor, $\bar{\Sigma}$, in Eq. (1) is an important aspect of the magnetosphere–ionosphere coupling process. In the LFM this tensor is

$$\bar{\Sigma} = \begin{pmatrix} \Sigma_P & \Sigma_H \\ -\Sigma_H & \Sigma_P \end{pmatrix}, \tag{2}$$

where Σ_P and Σ_H are the Pedersen and Hall conductivities. It includes a solar EUV contribution for the

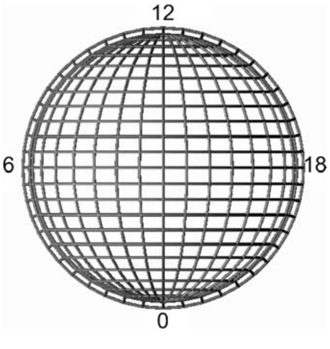

Fig. 1. A polar projection showing the ionospheric grid utilized within the LFM. The points within the grid result from the mapping of magnetospheric grid points at the inner boundary along dipole field lines to an ionospheric height of 100 km. The center of the ionospheric grid is aligned with the magnetic pole and the numbers around the edges indicate magnetic local time.

Pedersen

$$\Sigma_P = 0.5F_{10.7}^{2/3}\cos(\chi)^{2/3} \quad \chi \leqslant 65°, \tag{3}$$

$$\Sigma_P = \Sigma_P^{65°} - 0.12F_{10.7}^{2/3}(\chi - 65°) \quad 65° < \chi \leqslant 100°, \tag{4}$$

$$\Sigma_P = \Sigma_P^{100°} - 0.065F_{10.7}^{2/3}(\chi - 100°) \quad \chi > 100° \tag{5}$$

and Hall

$$\Sigma_H = 1.8F_{10.7}^{1/2}\cos(\chi) \quad \chi \leqslant 65°, \tag{6}$$

$$\Sigma_H = \Sigma_H^{65°} - 0.49F_{10.7}^{1/2}(\chi - 65°) \quad \chi > 65°, \tag{7}$$

conductances based upon fits to incoherent scatter radar data and has been used in AMIE studies (Richmond and Kamide, 1998). This model introduces a spatial varying conductivity profile based upon the solar EUV emission as represented by the 10.7 cm flux ($F_{10.7}$) as well as the instantaneous solar zenith angle (χ). This conductivity model allows for the inclusion of seasonal and diurnal variations into the coupling between the magnetosphere and ionosphere.

The other important contribution to the ionospheric conductivity is from precipitating energetic electrons. Since the empirical models used in determining the contribution to the Hall and Pedersen conductances plays an important role in the coupling with the TING model we will summarize the models presented in Fedder et al. (1995b).

The first step in calculating these conductances is to determine the characteristic energy and flux of the precipitating electrons. We begin by calculating an initial energy (ε_0),

$$\varepsilon_0 = \alpha c_S^2 \tag{8}$$

and thermal flux (F_0),

$$F_0 = \beta\rho\varepsilon_0^{1/2} \tag{9}$$

with c_s^2 as the sound speed and ρ as the density in the innermost cells of the magnetospheric grid. The constants α and β are chosen, based upon the work of Slinker et al. (1999), to obtain reasonable values for the precipitation energy into the ionosphere as well as adjusting the ionospheric conductivities to reasonable values.

The next step in the process uses the work of Chiu et al. (1981) to determine the field aligned electric potential energy difference between the inner edge of the magnetospheric grid and the ionosphere,

$$\varepsilon_\parallel = \frac{RJ_\parallel\varepsilon_0^{1/2}}{\rho}, \tag{10}$$

where R is another adjustable scaling factor for the parallel potential drop which includes an effective resistivity to FACs. As Chiu et al. (1981) notes this scaling factor is proportional to electron velocity and inversely proportional to electron density which means that for FACs out of the ionosphere the "hot" magnetospheric electrons must be drawn down resulting in a stronger electric field than is required to drawn the "cold" electrons out of the ionosphere in currents flowing into the ionosphere. In the LFM, we set R taken to be five times larger for current out of the ionosphere than for current into the ionosphere.

The final step in the determination of the flux and characteristic energy within the LFM uses the work of Orens and Fedder (1978) to account for the effects of the field aligned potential in the geomagnetic field. The final forms of the precipitating electron flux and energy are

$$F = F_0(8 - 7e^{-\varepsilon_\parallel/7\varepsilon_0}) \quad \varepsilon_\parallel > 0, \tag{11}$$

$$F = F_0 e^{\varepsilon_\parallel/\varepsilon_0} \quad \varepsilon_\parallel < 0 \tag{12}$$

and

$$\varepsilon = \varepsilon_0 + \varepsilon_\parallel. \tag{13}$$

The factors of 8 and 7 are related to the magnetic mirror ratio between the ionosphere and the altitude of the potential drop. In this formulation the characteristic energy of electrons is in keV and the electron number flux is in units of $\mathrm{cm^{-2}\,s^{-1}}$.

Once the final values for the flux (F) and energy (ε) are determined the ionospheric conductance model within the LFM, the work of Robinson et al. (1987) is used to determine the Pedersen,

$$\Sigma_P = \frac{5\varepsilon^{3/2}F^{1/2}}{(1.0 + 0.0625\varepsilon^2)} \tag{14}$$

and Hall,

$$\Sigma_H = 0.45\varepsilon^{0.85}\Sigma_P \tag{15}$$

conductances.

The magnetosphere–ionosphere coupling loop is completed by using the ionospheric solution for $\vec{E}$ as part of the boundary condition on the plasma flow at the inner boundary. The electric field is mapped back along dipole field lines used within,

$$\vec{v} = \frac{(-\nabla\Phi) \times \vec{B}}{B^2}. \tag{16}$$

as an equation for the plasma velocity boundary condition.

The LFM requires significant computational power to produce results in a reasonable amount of time. The typical time step is approximately 0.25 s, obtained through the utilization of the Borris correction (Borris, 1970) (see Lyon et al. (2004) for details on its implementation in the LFM). The OMP parallel version and the MPI based massively parallel version of the LFM can be run in near real time on 16 processors on an SGI-O2000 or eight processors of an IBM SP3.

2.2. The thermosphere ionosphere nested grid model

TING is a high resolution, three dimensional, time dependent model of the coupled thermosphere–ionosphere system. It is an extension of the NCAR TIGCM (Roble et al., 1998) used to study mesoscale processes in this system (Wang et al., 1999, 2004a). The model solves the coupled equations of mass continuity, momentum and energy for the neutrals and O^+ in the thermosphere and ionosphere. Chemical equilibrium is used to obtain the densities of the other ion species (NO^+, O_2^+, N_2^+, N^+) and the electrons. Details of the model can be found in Wang et al. (2004b) so we will only provide a brief summary of the model here concentrating on aspect which will be important for the coupling of TING with the LFM.

The basic grid for TING is a regular latitude and longitude grid which extends from −87.5° to 87.5° with 5° steps in latitude and steps longitude. As the name implies, TING has the capability for using nested grids in the latitude and longitude directions to concentrate resolution at regions of significant interest. The vertical grid extends from 97 to 500 km with 25 constant pressure levels.

The model has four primary inputs; (1) Solar EUV radiation, parameterized in terms of the $F_{10.7}$ flux, (2) auroral particle precipitation characterized in terms of the characteristic energy and number flux, (3) imposed magnetospheric electric field at high latitudes, and (4) tides from the lower atmosphere. In stand-alone operation these parameters are determined from empirical models characterized by indices like K_p or by the solar wind conditions (Wang et al., 2001).

TING provides several output parameters that are not possible to determine from the simple ionospheric model used within the LFM and are important for space weather applications. The model can be used to predict the electron and ion temperatures and densities as well as the commonly measured quantities like Total Electron Content (TEC), density of the F2 peak (NmF2), and height of the F2 peak (HmF2). It also provides information about the behavior of the neutral thermosphere.

The computational requirements of the TING model are quite modest when compared with the LFM. The typical time step of the model is 2 min and takes a small fraction of that time to complete the step on a single processor of a high end massively parallel supercomputer or Linux PC.

2.3. Model coupling methodology and implementation

Fig. 2 shows a schematic representation of the coupling process between the LFM and TING to form the CISM CMIT Model. The model is broken down into three component parts. The LFM model, which for the purposes of this diagram is limited to the magnetospheric portion of the simulation. The magnetosphere–ionosphere (MI) coupler which includes the ionospheric portion of the LFM model and infrastructure for communicating between the LFM and TING models. As a practical matter the code for the MI coupler is embedded within the LFM. The TING model is essentially the same program as the stand alone TING module with infrastructure added for communicating with the MI coupler.

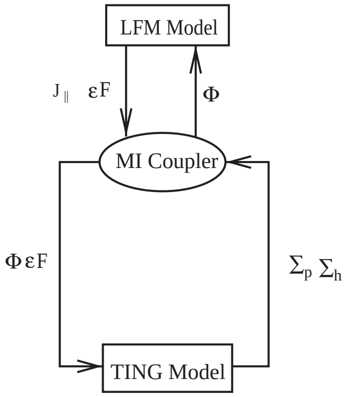

Fig. 2. Schematic representation of the LFM TING coupling process. Arrows represent data flow with parameters passed between modules indicated next to each arrow.

Two of the four inputs to the TING model, the auroral particle precipitation and the ionospheric electric field, are determined by the empirical relationships used within the LFM ionospheric model. During the first exchange with TING the MI coupler uses relationships for the characteristic energy and flux of the precipitating electrons in Eqs. (14) and (15) to make an initial determination of the ionospheric electric field. The MI coupler then makes the UT dependent transformation of the these parameters from the LFM ionospheric grid to the TING grid and waits for the TING model to complete its determination of the height integrated Hall and Pedersen conductivities. The details on how these conductivities are calculated are described in more detail in Wang et al. (2004b). Once the conductivities have been determined the information is used to recompute the electric field via Eq. (1). This new electric field is passed back to the magnetospheric portion of the LFM as part of its inner boundary condition.

The large disparity in computational time between the LFM and TING models brings up another important aspect of the coupling between these models. During the 2 min interval between exchanges of information between the MI coupler and the TING model the LFM needs revised ionospheric electric fields. In this time frame the MI coupler uses the conductances from the previous step to compute the electric field based upon the current field aligned currents. The current implementation has the MI coupler waiting for the TING model to complete its work before proceeding, but it would be a simple matter to have this process executing concurrently with the LFM and have the MI coupler lag one data exchange behind in the information it uses for the Hall and Pedersen conductivities. This coupling approach results in a consistent set of conductances and electric fields being used within both components of the CISM CMIT model. At this time the coupling methodology uses a series of lock and data transfer files to create a fully automatic mechanism for communications between the components of CMIT.

Another aspect of MI coupling which is not currently included in the CISM CMIT model is the effect of the ionospheric dynamo current, $J_{\|\mathrm{I}}$ on the ionospheric electric field. According to the basic ionospheric physics described in Kelly (1989) this current is

$$J_{\|\mathrm{I}} = -\nabla \cdot \int_h \bar{\sigma} \cdot (\vec{U} \times \vec{B})\,\mathrm{d}h, \tag{17}$$

where h is the height of the ionosphere, $\vec{U}$ is the neutral velocity, $\bar{\sigma}$ is the conductivity tensor, $\vec{B}$ is the magnetic field, and $J_{\|\mathrm{I}}$ is the ionospheric dynamo current. Including this effect results in

$$\nabla_\perp \cdot \bar{\Sigma} \cdot \nabla_\perp \Phi = J_\| - J_{\|\mathrm{I}} \tag{18}$$

as a new version of the ionospheric electric field equation replacing Eq. (1) in the MI coupler. The inclusion of this term will allow the ionospheric flywheel effect to couple into the magnetosphere after strong storm periods, but will be negligible most of the time (Richmond and Roble, 1987; Ridley et al., 2003).

In summary, the effect of this coupling to the LFM is the replacement of the empirical determination of the Hall and Pedersen conductivities with the first principle calculations present in the TING model. It also allows for the inclusion of the ionospheric dynamo effect. As far as the TING model goes the coupling allows for the replacement of parameterized models for ionospheric electric field and aurora precipitation with parameters determined with a higher time resolution by the LFM.

3. Results from climatology studies

In order to study the two way coupling between the thermosphere–ionosphere and the magnetosphere three sets of simulations where completed: (1) the LFM with its standard empirical ionosphere, (2) a TING run with empirical magnetospheric inputs, and (3) the fully coupled CISM CMIT model. In each simulation used the same set of idealized solar wind conditions shown in Fig. 3. These conditions hold the solar wind velocity and density constant at 400 km/s and 5 #/cc, respectively during the entire interval. The B_X GSM component of the IMF is set to zero. The LFM begins with approximately 50 min of solar wind with no IMF to distort the initial dipole magnetic field into the shape of the magnetosphere. The IMF is then turned southward to complete initialization the magnetospheric portion of the simulation. During the initialization period the LFM uses its standard model for the ionosphere. The TING model is run for three days to create a diurnally reproducible state appropriate for the geophysical conditions present at the beginning of the interval coupling which begins at 1230 UT. At 1430 UT the IMF is turned northward ($B_Z = 5$ and $B_Y = 0\,\mathrm{nT}$) for a period of 4 h. The IMF and then becomes eastward ($B_Z = 0$ and $B_Y = 5\,\mathrm{nT}$), southward ($B_Z = -5$ and $B_Y = 0\,\mathrm{nT}$), and westward ($B_Z = 0$ and $B_Y = -5\,\mathrm{nT}$) for 4 h intervals. Since the transformation between the LFM ionospheric grid and the TING geographic grid is dependent upon date and we chose May 19, 1996 as the starting date for these simulations.

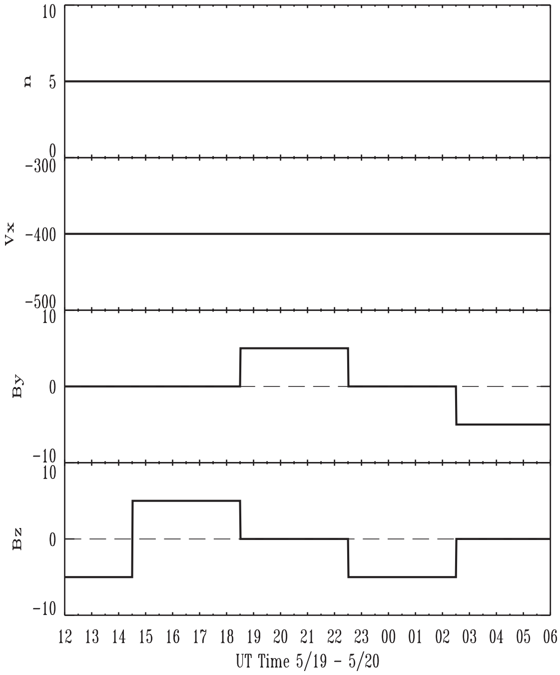

Fig. 3. The solar wind conditions used for both the LFM and the coupled CISM CMIT runs. After an initial period of southward IMF the magnetic field is rotated through the four clock angle directions for a period of four hours while the solar wind velocity and density are held constant.

Fig. 4 shows a comparison between the LFM and the CISM CMIT models for the northern hemisphere cross polar cap potential during the entire run. The results for the LFM are shown with the thin black line while values for the CISM CMIT model are shown with the thick

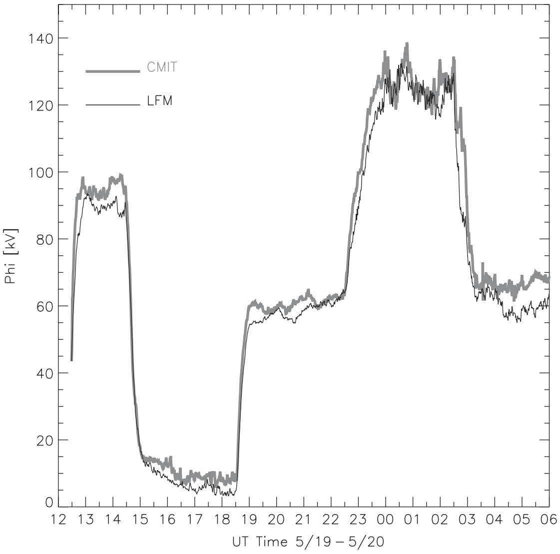

Fig. 4. The cross polar cap potential for the entire interval is shown. The LFM results are shown with the thin black line while the CISM CMIT results are shown with the thick grey line.

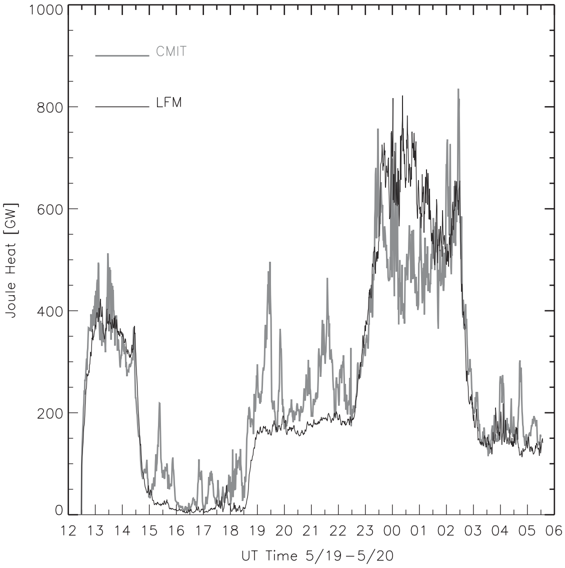

Fig. 5. The northern hemisphere joule heating for the entire interval is shown. The LFM results are shown with the thin black line while the CISM CMIT results are shown with the thick grey line.

grey line. Initial inspection of the model results shows that there is excellent qualitative agreement in the cross polar cap potential between both of the models, with the CISM CMIT model have a consistently higher value for the potential. During the period of northward IMF, the LFM has an average value of 7.3 kV while the CISM CMIT model has an average value of 12.2 kV a difference of 4.9 kV or 40%. When the IMF is eastward the average values are 58.7 and 60.3 kV for the LFM and CMIT models which is a difference of only 2.6%. The difference between models during the period westward IMF increases to roughly 9% which is probably due to in large part the increased activity during the preceding period of southward IMF, but may also be a reflection of the change in the dipole tilt angle. In the period of southward IMF both models show significant variability in the cross polar cap potential value initially due to the time required to increase convection and then later to magnetospheric variability including a small substorm. The average values during the period of sustained enhanced convection of 124.5 kV for the LFM and 126.0 kV for the CMIT model differ by less than 1%. The coupled model reaches the average value of potential fifteen minutes quicker than the uncoupled version. We interpret the relatively small disparity between the models during the entire run as indicative of an accurate and stable coupling of the LFM and TING.

A comparison for the northern hemisphere Joule heating between the two models is shown in Fig. 5 which uses the same format as Fig. 4. The Joule heating was calculated by computing $\vec{J}_{\perp} \cdot \vec{E}$ in the 2D ionospheric grid within the MI coupler. While this comparison shows a general qualitative agreement between the models, it also shows the first indications of interesting differences in the physical response of the system. It is quite clear that the CISM CMIT model shows significantly more variability during the entire interval, especially during the periods of northward and eastward IMF, with numerous peaks in the Joule heating which are not present in the LFM simulation. In addition, the average amount of Joule heating seen in the coupled model during the southward IMF interval is 142 GW less than was seen in the uncoupled model. Both of these features are indicative of ionospheric and thermospheric processes which are not included in simple ionosphere used by the LFM.

The east–west currents in the ionosphere produce a simple proxy for AL in the simulation using the maximum value the current in a sector centered around midnight as the source for the current term in Ampere's Law. In order to simplify the comparison, the height integrated conductivities were used to calculate the ionospheric currents in both models with results being shown in Fig. 6. During the periods of northward and eastward IMF both models show very low levels of activity. After the southward turning of the IMF both models show the classic indications of the a substorm growth phase followed by a clear onset. The 00 UT onset in the LFM is more abrupt than the CISM CMIT model which shows a more rapid increase in current strength prior to the 00 UT onset. The coupled model produces a

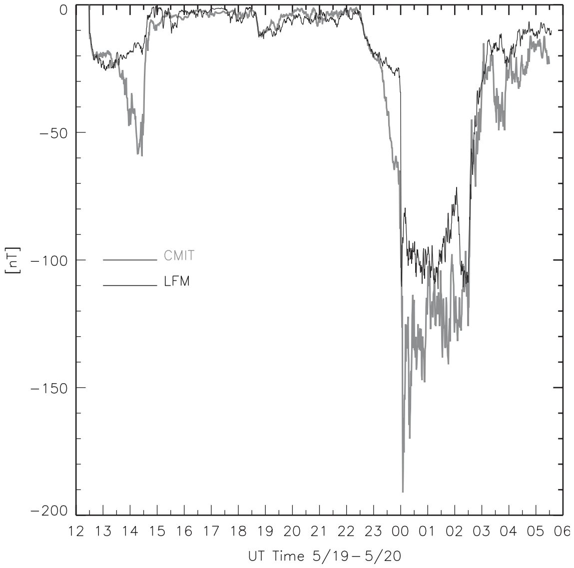

Fig. 6. The simulated AL for the entire interval is shown. The LFM results are shown with the thin black line while the CMIT results are shown with the thin grey line.

much larger peak followed by a rapid initial recovery phase, while the LFM appears to reach a sustained level of activity for about an hour before showing signs of decreased activity. Both models have increased AL up until the IMF turns westward, at which time they both decrease in intensity. The coupled model has a small period of increased activity shortly after the IMF changes direction which is not seen in the LFM. The stronger AL in the CISM CMIT model is due to the presence of larger Hall currents. It is quite interesting to note that both models have the same onset time even though the method for determining the conductivities is dramatically different.

So far the comparison between the LFM and the CISM CMIT model has been limited to global features like the cross polar cap potential and joule heating. In Figs. 7 and 8 we present a series of panels which show the structure of the ionosphere during the various IMF conditions. The top panel in Fig. 7 was taken from the simulations at 18 UT near the end of the period of northward IMF. The bottom panel was taken at 22 UT during the period of eastward IMF; 02 UT was used as the reference time for the southward IMF period shown in the top panel of Fig. 8. The bottom panel of Fig. 8, during westward IMF, was taken at 06 UT. In each panel the results from the LFM are shown on the left with the CISM CMIT results being shown in the right column.

Within each section of Figs. 7 and 8 the display is broken down into six different magnetic local time grids with noon at the top of the display and magnetic latitudes of 45, 60, and 75° indicated. The structure of the ionospheric potential pattern is shown in the upper left with contours ranging from -60 to 60 kV with a 5 kV interval for each IMF condition, except northward IMF when the interval was reduced to -10–10 kV with a 1 kV contour interval to allow the structure of the four cell convection pattern to be displayed. In the upper middle plot the structure of the field aligned currents into the ionosphere are displayed with contours from -1 to 1 $\mu A/m^2$ at 0.2 $\mu A/m^2$ spacing. Once again during northward IMF the contour resolution had to be increased, -0.25 to 0.25 $\mu A/m^2$ with a 0.05 $\mu A/m^2$ spacing, to allow for visualization of the NBZ current system. The upper right plot shows the Pedersen conductivity from 0 to 12 S with a 1 S interval. Directly underneath the Pedersen conductivity the structure of Hall conductivity is displayed with the same contours. In the lower left corner the characteristic energy, ε, of electrons precipitating into the ionosphere is display with contours every 0.5 keV from 0 to 15 keV. The number flux, F, of precipitating electrons is shown in the lower middle contour plot with contours every $1 \times 10^7\,cm^{-2}\,s^{-1}$ from 0 to $3 \times 10^8\,cm^{-2}\,s^{-1}$. Except for the northward IMF potential and current contour plots the contour intervals are the same for each of parameters at all times. The contour intervals are always the same between LFM results and the CISM CMIT model.

The northward IMF portion of Fig. 7 shows a classic four cell convection pattern driven by an NBZ current system. The location and strength of the NBZ current system is very close between the two model results, with the CISM CMIT model having slightly smaller area for the main current system. Each potential pattern shows the classic four cell convection pattern, but the CISM CMIT model shows signs of a much larger viscous interaction region at low latitudes along the dusk and dawn flanks. The weak precipitation effects do not produce significant levels of auroral conductivity enhancement in either model. The background EUV Pedersen conductivity has the same maximum value and a clear local time dependence can be seen in the conductivities coming back from TING which is not present in the EUV model used with the LFM ionospheric module. The same local time variations can be seen in the comparison between the Hall conductivities. This variation is also compounded by the fact that the maximum Hall conductivity in the LFM is 14 S while the maximum conductivity in the CISM model is only 10 S. The qualitative agreement between these to simulations during northward IMF is quite strong.

In the bottom panel of Fig. 7 the structure of ionosphere at 22 UT (eastward IMF) in the LFM and CISM CMIT Model is compared. Both models show two cell convection patterns with a larger dusk cell as expected for eastward IMF (Weimer, 2001). The current patterns also show very strong similarities between the models. Even though the peak flux in the LFM is higher

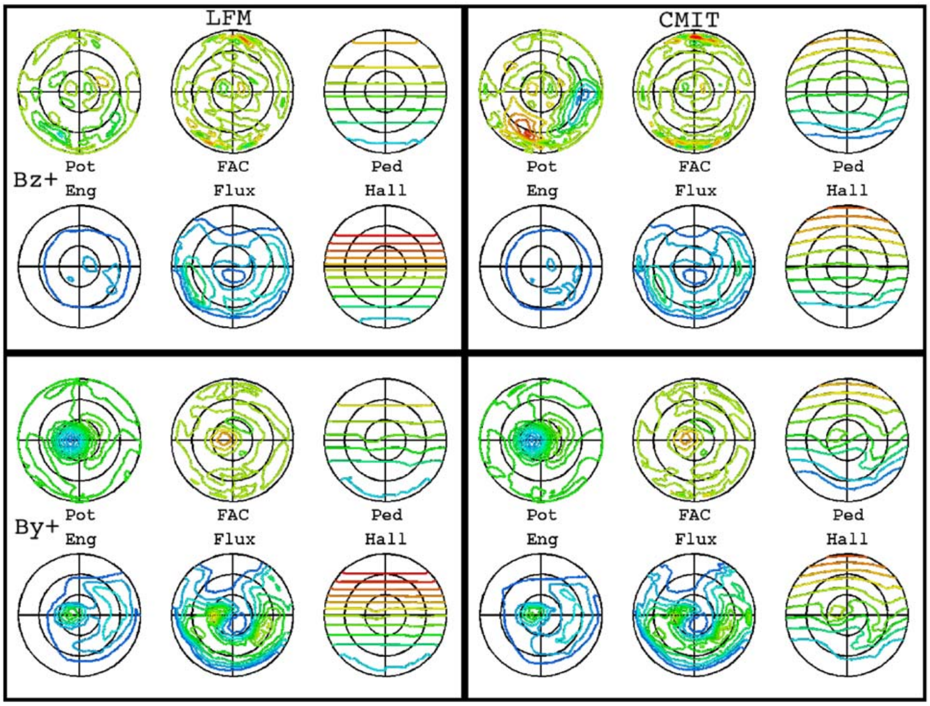

Fig. 7. Ionospheric structure comparison between the LFM (left) and the CISM CMIT (right) results at 18 UT (top) during northward IMF and at 22 UT (bottom) during eastward IMF.

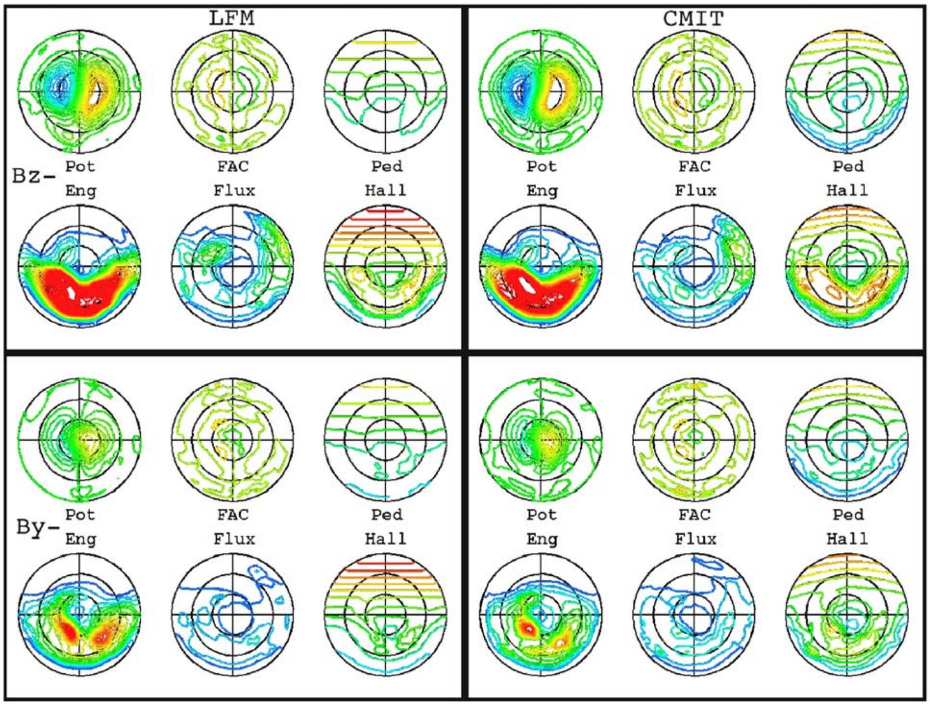

Fig. 8. Ionospheric structure comparison between the LFM (left) and the CISM CMIT (right) results at 02 UT (top) during southward IMF and at 06 UT (bottom) during westward IMF.

than seen in the coupled model the resulting Hall and Pedersen conductivity patterns do not show significant effects of particle precipitation. Both the Pedersen and Hall conductivity patterns in the CMIT model have an enhanced auroral zone pattern, especially in the post midnight to dawn sector, as well as stronger conductivity in the strong downward current driving the convection pattern. The presence of a more clearly defined auroral zone is more representative of observations during these conditions then the results from the ionospheric portion of the LFM.

At 02 UT the ionosphere is well into the recovery phase of the substorm which occurred at 00 UT in both simulations. The state of the ionosphere is shown in the top panel of Fig. 8. Once again both models show very similar convection and field aligned current patterns. CMIT has a stronger dawn side cell which is contributing to the larger cross polar cap potential seen in Fig. 4. In this case the LFM clearly shows the effects of particle precipitation on the conductivities. A clear auroral zone is seen with the strongest conductivities occurring in the post midnight sector as is expected for the recovery phase of a substorm. CMIT shows similar features in the conductivity, with the exception that the peak Hall conductivity in the auroral zone comparable to the maximum of the solar EUV conductivity. It is also a few mhos larger than the Hall conductivity seen the LFM auroral zone. Once again we see qualitative agreement between the two models with important structures like the auroral zone being more consistent with observations and empirical models in the coupled model.

The bottom panel of Fig. 8 shows the state of the ionosphere in both models during the westward IMF period at 06 UT. Both models show two-cell potential patterns with the dawn cell being larger. In the LFM the upward FAC covers a slightly larger area than the same current system in CMIT. In addition, the region of higher energy precipitating electrons is also larger in the LFM. The conductivities show a dissipating auroral zone which includes the effects of the westward IMF as well as the previous period of enhanced activity.

The majority of this paper has concentrated on the comparison between the ionospheric response in the two models. Fig. 9 shows the structure of the magnetosphere at the time of the substorm onset in the simulations. The top panel is from the LFM while the bottom panel is from CMIT. In each panel a cut through the *XZ* plane is colored with the log of the plasma density using the same color range for each simulation. The panels also show the surface composed of the last closed field lines. It is very clear from the plasma distribution that for the vast majority of the magnetosphere there is little or no difference between the simulation results. In addition, both simulations place the magnetopause at $10R_\mathrm{E}$, show similar shape and density within the lobes and plasma sheet. The most notable difference between the simulations is in the tailward extent of the last closed field line surface which is approximately $4R_\mathrm{E}$ further Earthward in the CMIT model then the in the LFM. This difference is probably the results of the larger substorm seen in the ionospheric portion of the CMIT results. The high level similarity between the two models' magnetospheric structure occurs throughout the entire simulation.

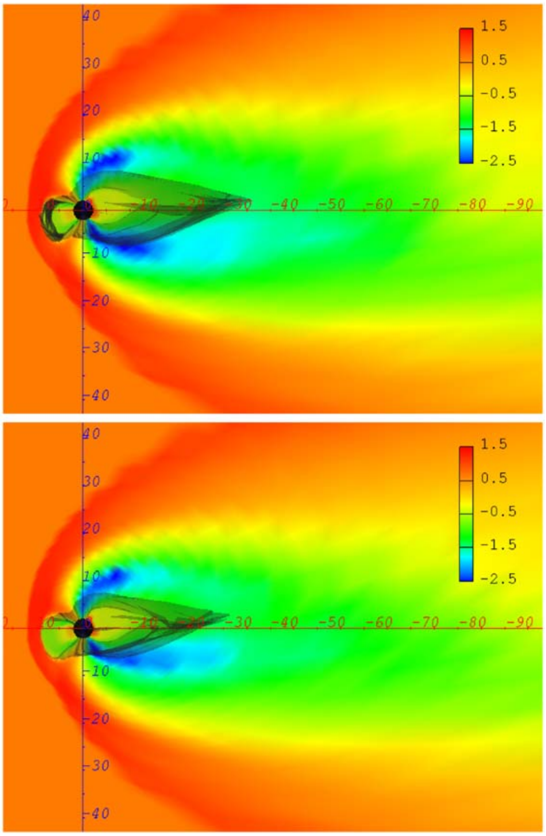

Fig. 9. Snapshots depicting the state of the magnetosphere at 00 UT, the time of substorm onset, in both the LFM and CMIT Models. The LFM is on top with CMIT directly underneath. In each panel the background shows the log of the plasma density on the same color scale. The grey transparent feature is the surface composed of the last closed field lines.

4. Discussion and conclusions

In this work we have presented the results from an idealized set of solar wind conditions used to drive the LFM and the CISM CMIT models. The coupled model produces essentially the same cross polar cap potential and AL indices, but show significantly more time variability in the ionospheric Joule heating. The structure of the ionospheric conductances, energy flux, field aligned currents, and cross polar cap potential are in qualitative agreement. These results show that the coupled model is working well.

As previously noted, the structure of the ionospheric conductivities is in qualitative and reasonable quantitative agreement under all four IMF conditions. The CMIT results show a more clearly defined ionospheric auroral oval than the empirical approximation used with LFM produces. This is especially true during the weak driving present in the eastward and westward IMF. In addition, there appears to be a significant spatial variation in the EUV conductance patterns. The local time features seen in both Pedersen and Hall conductivities during northward IMF are clearly the result of a more accurate means of dealing with the solar zenith angle then the simple relationship presented in Eqs. (3)–(8). The difference between the maximum Hall conductivities is not completely understood, but maybe the result of the very high values of characteristic energy for precipitating electrons coming from the empirical model used within the LFM. The peak values of 15 keV seen during the southward IMF interval are much higher than the 5 keV values seen under the $K_p = 6$ conditions of the Hardy et al. (1985) statistical study of precipitation. These high energies will mainly effect the Hall conductivities and are probably the source of the significant differences in the Hall conductivities between the LFM and CISM CMIT model. Further runs will be required to adjust the parameters in the empirical model to reduce the high values during southward IMF, but maintain reasonable values seen during other IMF conditions.

Its important to note that both LFM and the CISM CMIT models produces values for the cross polar cap potential which are much higher than those seen by observations (Rich and Hairston, 1995; Shepherd et al., 2002) or those produced by empirical models (Boyle et al., 1997) for similar conditions. The Boyle relationship predicts a value of 75 kV for the southward IMF period which is a factor of 0.6 times smaller than the average value obtained from either model. During eastward and westward IMF the models produce potentials which differ by a similar factor. It is interesting to note that the LFM and CMIT models produce a potential which is smaller than the Boyle prediction for northward IMF. The high values for the ionospheric potential in LFM simulations of the magnetosphere is not a new result. One possible explanation is the LFM does not produce Region 2 currents which are comparable in magnitude with those occurring in nature. The lack of Region 2 currents results in a high polar cap potential (Korth et al., 2004). Comparing the CMIT model with field aligned current observations made by Iridium (Anderson et al., 2000) in conjunction with either SuperDARN potential patterns or conductivities inferred from POLAR will be required to more accurately isolate the cause of this problem.

In conclusion, the comparison of global measurements as well as ionospheric and magnetospheric structure leads us to believe that we have successfully coupled the LFM with TING to create the CISM CMIT model. Within the magnetosphere the change from an empirical to a first principles derivation of the ionospheric conductivities has not resulted in significant changes in the structure of the magnetosphere. This result is not surprising since the changes in the structure of ionospheric conductivities have not been profound. The ionospheric model included in CMIT is height resolved and includes first principles physics not found within the stand alone LFM. In addition, this coupling will allow us to include the effects of thermospheric neutral wind driven currents which is not possible within the LFM. The coupled model can now be used to conduct event based validation studies as well as investigations into the physics of the driving of the ionosphere-thermosphere system by the magnetosphere.

Acknowledgements

This material is based upon work supported in part by CISM, which is funded by the STC Program of the National Science Foundation under Agreement Number ATM-0120950. The National Center for Atmospheric Research is sponsored by the National Science Foundation. We would also like to thank Steve Slinker for his helpful conversations.

The Editor would like to thank the reviewers of this manuscript.

References

Anderson, B.J., Takahashi, K., Toth, B.A., 2000. Sensing global birkeland currents with iridium engineering magnetometer data. Geophysical Research Letters 27, 4045–4048.

Borris, J.P., 1970. A physically motivated solution of the Alfven problem. Technical Report 2167. Naval Research Laboratory, Washington, DC.

Boyle, C.P., Reiff, P.H., Hairston, M., 1997. Empirical polar cap potentials. Journal of Geophysical Research 102, 111–125.

Chen, F.F., 1984. Introduction to Plasma Physics and Controlled Fusion, second ed. Plenum, New York.

Chiu, Y.T., Newman, A.L., Cornwall, J.M., 1981. On the structures and mapping of auroral electrostatic potentials. Journal of Geophysical Research 86, 10029.

Fedder, J.A., Lyon, J.G., 1987. The solar wind–magnetosphere–ionosphere current–voltage relationship. Geophysical Research Letters 8, 880.

Fedder, J.A., Lyon, J.G., 1995. The Earth's magnetosphere is $165R_E$ long: self-consistent currents, convection, magnetospheric structure, and processes for northward interplanetary magnetic field. Journal of Geophysical Research 100, 3623.

Fedder, J.A., Lyon, J.G., Slinker, S.P., Mobarry, C.M., 1995a. Topological structure of the magnetotail as function of interplanetary magnetic field and with magnetic shear. Journal of Geophysical Research 100, 3613.

Fedder, J.A., Slinker, S.P., Lyon, J.G., Elphinstone, R.D., 1995b. Global numerical simulation of the growth phase and the expansion onset for substorm observed by Viking. Journal of Geophysical Research 100, 19083.

Fuller-Rowell, T.J., Codrescu, M.V., Moffeff, R.J., Quegan, S., 1994. Response of the thermosphere and ionosphere to geomagnetic storms. Journal of Geophysical Research 99, 3893–3914.

Gombosi, T.I., DeZeeuw, D.L., Groth, C.P.T., Powell, K.G., Song, P., 1998. The length of the magnetotail for northward IMF: results from 3d MHD simulations. In: Chang, T., Jasperse, J.R. (Eds.), Physics of Space Plasmas, vol. 15. AGU, Washington, DC, p. 121.

Goodrich, C.C., Wiltberger, M., Lopez, R.E., Papadopoulos, K., Lyon, J.G., 1998. An overview of the impact of the January 10–11, 1997 magnetic cloud on the magnetosphere via global MHD simulation. Geophysical Research Letters 25, 2537–2540.

Hain, K., 1977. Behavior of ionized plasma in the high latitude topside ionosphere. NRL Memo Report 3713, 1.

Hain, K., 1987. The partial donor method. Journal of Computational Physics 73, 131.

Hardy, D.A., Gussenhoven, M.S., Holeman, E., 1985. A statistical model of auroral electron precipitation. Journal of Geophysical Research 90, 4229–4248.

Janhunen, P., 1996. GUMICS-3—a global ionosphere–magnetosphere coupling simulation with high ionospheric resolution. The ESA Symposium on Environment Modeling for Space-Based Applications. ESA, Paris.

Kelly, M.C., 1989. The Earth's Ionosphere: Plasma Physics and Electrodynamics. Academic Press, San Diego.

Korth, H., Wiltberger, M., Anderson, B.J., Lyon, J.G., Anderson, P.C., 2004. Intercomparison of ionospheric electrodynamics from the Iridium constellation with global MHD simulations. J. Geophys. Res. 109, A07307, doi: 10.1029/2004JA010428.

Luhman, J., Solomon, S., Wang, W., Wiltberger, M., 2004. The center for integrated space weather modeling. Journal of Atmospheric and Solar Terrestrial Physics, this issue.

Lyon, J., Lopez, R.E., Goodrich, C., Wiltberger, M., Papadopoulos, K., 1998. Simulation of the March 9, 1995 substorm: auroral brightening and the onset of lobe reconnection. Geophysical Research Letters 25, 3039–3042.

Lyon, J.G., Fedder, J.G., Mobarry, C.M., 2004. The Lyon–-Fedder–Mobarry (LFM) global MHD magnetospheric simulation code. Journal of Atmospheric Space Physics, this issue.

Mobarry, C., Fedder, J.A., Lyon, J.G., 1996. Equatorial plasma convection from global simulations of the Earth's magnetosphere. Journal of Geophysical Research 101, 7859.

Odstrcil, D.J., Linker, J.A., Lionello, R., Mikic, Z., Riley, P., Pizzo, V.J., 2002. 3d MHD simulations of CMEs by coupled coronal and heliospheric models. In: Wilson, A. (Ed.), Proceedings of the 10th European Solar Physics Meeting, Paris. ESA, pp. 95–98.

Orens, J.H., Fedder, J.A., 1978. The effects of geomagnetic field aligned potential difference on precipitating magnetospheric particles. NRL Memo Report 3573.

Raeder, J., 1999. Modeling the magnetosphere for northward interplanetary magnetic field: effects of electrical resistivity. Journal of Geophysical Research 104, 17357.

Raeder, J., McPherron, R.L., 1998. Global MHD simulations of the substorm current wedge and dipolarization. In: The Fourth International Conference on Substorms. Kluwer Academic Publishers, Dordrecht, The Netherlands, p. 334.

Raeder, J., Wang, Y., Fuller-Rowell, T.J., 2001. Geomagnetic storm simulation with a coupled magnetosphere–ionosphere–thermosphere model. In: Song, P., Singer, H., Siscoe, G. (Eds.), Space Weather, Geophysical Monograph Series, vol. 125. AGU, Washington, DC, pp. 377–384.

Rich, F.J., Hairston, M., 1995. Large-scale convection patterns observed by DMSP. Journal of Geophysical Research 99, 3827.

Richmond, A.D., 1992. Assimilative mapping of ionospheric electrodynamics. Advances in Space Research 12, 59–68.

Richmond, A.D., Kamide, Y., 1998. Mapping electrodynamic features of the high latitude ionosphere from local observations. Journal of Geophysical Research 93, 5741.

Richmond, A.D., Roble, R.G., 1987. Electrodynamic effects of thermospheric winds for the NCAR thermospheric general circulation model. Journal of Geophysical Research 92, 12365.

Richmond, A.D., Ridley, E.C., Roble, R.G., 1992. A thermosphere/ionosphere general circulation model with coupled electrodynamics. Geophysical Research Letters 19, 601.

Ridley, A.J., Richmond, A.D., Gombosi, T.I., Clauer, C.R., 2003. Ionospheric control of magnetospheric configuration: thermospheric neutral winds. Journal of Geophysical Research 108 doi:10.1029/2002JA009.

Robinson, R.M., Vondrak, R.R., Miller, K., Babbs, T., Hardy, D.A., 1987. On calculating ionospheric conductivities from the flux and energy of precipitating electrons. Journal of Geophysical Research 92, 2565.

Roble, R.G., Ridley, E.C., 1994. A thermosphere–ionosphere–mesosphere–electrodynamics general circulation model (TIME-GCM): equinox solar minimum simulations (30–500 km). Geophysical Research Letters 21, 417–420.

Roble, R.G., Ridley, E.C., Richmond, A.D., Dickenson, R.E., 1998. A coupled thermosphere/ionosphere general circulation model. Geophysical Research Letters 15, 1325.

Shepherd, S.G., Greenwald, R.A., Ruohoniemi, J.M., 2002. Cross polar cap potentials measured with super dual auroral radar network during quasi-steady solar wind and interplanetary magnetic conditions. Journal of Geophysical Research 107 doi:10.1029/2001JA000152.

Siscoe, G.L., Crooker, N.U., Erickson, G.M., Sonnerup, B.U., Siebert, K.D., Weimer, D.R., White, W.W., Maynard, N.C., 2000. Global geometry of magnetospheric currents. In: Ohtani, S.I. (Ed.), Magnetospheric Current System, Geophysical Monograph Series, vol. 118. AGU, Washington, DC, pp. 41–52.

Slinker, S.P., Fedder, J.A., Emery, B.A., Baker, K.B., Lummerzheim, D., Lyon, J.G., Rich, F.J., 1999. Comparison of global MHD simulations with AMIE simulations for the events of May 19–20, 1996. Journal of Geophysical Research 104, 28379.

Wang, W., Killeen, T.L., Burns, A.G., Roble, R.G., 1999. A high-resolution, three-dimensional, time-dependent, nested grid model of the coupled thermosphere–ionosphere. Journal of Atmospheric and Solar Terrestrial Physics 61, 385–397.

Wang, W., Killeen, T.L., Burns, A.G., Reinisch, B.W., 2001. A real time model-observation comparison of f_2 peak electron densities during the Upper Atmospheric Research Collaboratory campaign of October 1997. Journal of Geophysical Research 106, 21077.

Wang, W., Burns, A.G., Solomon, S., Killeen, T.I., 2004a. High resolution, coupled thermosphere–ionosphere models for space weather applications. Advances in Space Research, in press.

Wang, W., Wiltberger, M., Burns, A.G., Solomon, S., Killeen, T.I., 2004b. Initial results from the center for integrated space weather modeling coupled magnetosphere ionosphere thermosphere model: ionospheric and thermospheric responses. Journal of Atmospheric and Solar Terrestrial Physics, this issue.

Weimer, D.R., 2001. Models of high-latitude electric potentials derived with a least error fit of spherical harmonic coefficients. Journal of Geophysical Research 100, 19595–19607.

Wiltberger, M., Pulkkinen, T.I., Lyon, J.G., Goodrich, C.C., 2000. MHD simulation of the December 10, 1996 substorm. Journal of Geophysical Research 106, 27649–27663.

Wiltberger, M., Lyon, J.G., Goodrich, C.C., 2003. Results from the Lyon–Fedder–Mobarry global magnetospheric model for the electrojet challenge. Journal of Atmospheric and Solar Terrestrial Physics 65, 1213–1222.